Railway wheel failure caused by flange crack, part 2: Fatigue and fracture assessment

Downloaded from: https://research.chalmers.se, 2026-05-05 20:39 UTC

Citation for the original published paper (version of record):
Ekberg, A., Vernersson, T., Hjertsén, D. (2026). Railway wheel failure caused by flange crack, part 2: Fatigue and fracture assessment. Engineering Failure Analysis, 193.
http://dx.doi.org/10.1016/j.engfailanal.2026.110880

N.B. When citing this work, cite the original published paper.

research.chalmers.se offers the possibility of retrieving research publications produced at Chalmers University of Technology. It covers all kind of research output: articles, dissertations, conference papers, reports etc. since 2004. research.chalmers.se is administrated and maintained by Chalmers Library

(article starts on next page)

Engineering Failure Analysis 193 (2026) 110880

Contents lists available at ScienceDirect

Engineering Failure Analysis

journal homepage: www.elsevier.com/locate/engfailanal

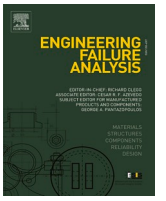

Railway wheel failure caused by flange crack, part 2: Fatigue and fracture assessment

Anders Ekberg [a,*], Tore Vernersson [a], David Hjertsén [b]

[a] CHARMEC, Chalmers University of Technology, SE 412 96 Gothenburg, Sweden
[b] Element Materials Technology, ASJ-vägen 7, SE 582 54 Linköping, Sweden

ARTICLE INFO

Keywords:
Railway
Derailment
Fatigue
Tread braking
Wheel fracture
Thermal stresses

ABSTRACT

Causes of a wheel fracture resulting in a derailment that caused major traffic disruptions and costs are investigated based on findings in the first part of this paper [1]. Numerical finite element (FE) simulations together with a fatigue initiation assessment indicate that the fatigue crack at the inside of the flange that triggered the wheel fracture was caused by a combination of wheel–rail contact loads during curving and tensile residual stresses caused by previous overheating of the flange. A fracture mechanics-based analysis is carried out to establish the plausibility of this hypothesis by estimating fatigue crack growth rates and load magnitudes required to cause the final fracture. In order to further assess the influence of flange overheating, the residual stress field is evaluated in a thermomechanical viscoplastic FE-simulation and mapped onto a FE-based fracture mechanics model of the loaded flange crack using an innovative genetic algorithm approach.

The study establishes root causes of the fatigue failure to be a combination of high mechanical stresses due to heavy haul operations with worn wheel profiles, and tensile residual stresses caused by prior heating of the flange by a misaligned brake block. Further, scratches on the inside of the flange have acted as crack initiators. Although it is not possibly to evaluate an exact crack growth life due to uncertainties in load magnitudes, the position of crack initiation in relation to the evaluated stress field together with crack growth rate estimations indicate that crack growth started before the previous reprofiling twenty-one months before the derailment.

1. Introduction

A fully loaded iron ore train on route from Kiruna in Sweden to Narvik in Norway derailed at Vassijaure station on the 17th of December 2023 [2]. Investigations [1] revealed the cause of the detached wheel to be a radial fracture induced by a fatigue crack on the inside (towards centre of the track) of the flange and extending to the hub, see Fig. 1. This caused a wheel of type BLS 32.5 [2] to loosen its grip on the axle, which allowed the wheel to traverse laterally. Due to this, some 15 km of track was damaged as one wheel was rolling on the inside of the rail before final derailment due to switch negotiation.

In the first part of the investigation [1], fracture characteristics were evaluated and wheel rim geometries established. The initial crack was identified as the crack shown in Fig. 1. In addition, blueing of the wheel, see Fig. 2, together with wear of a detached brake shoe indicated brake shoe heating of the flange, a hypothesis that was further strengthened through tests by the operator that showed

* Corresponding author.
E-mail address: anders.ekberg@chalmers.se (A. Ekberg).

https://doi.org/10.1016/j.engfailanal.2026.110880
Received 7 November 2025; Received in revised form 11 March 2026; Accepted 13 April 2026
Available online 15 April 2026
1350-6307/© 2026 The Author(s). Published by Elsevier Ltd. This is an open access article under the CC BY license (http://creativecommons.org/licenses/by/4.0/).

the brake block support to be flexible in the lateral direction. Further, material and mechanical characteristics of the failed wheel were established and compared to specifications. No significant deviations were found.

This part of the investigation consists of an assessment of load conditions likely to have triggered fatigue initiation, crack growth and final fracture. Here the geometry of the fatigue crack in Fig. 1 serves as a key input. In addition, the brake shoe worn in contact with the flange that was found in the on-site failure investigation implies that there had been an abnormal thermal frictional loading of the flange.

The current type of failure cannot really be characterised as rolling contact fatigue (cf. [3,4]), nor as thermal cracking (cf. [5]). The reason is that the crack is not initiated/propagated in the contact stress field but driven by cyclic tensile stresses on the inside of the flange. Although it is found to be promoted by tensile residual stresses due to flange overheating it is not a thermal crack in the sense that the mechanical load is the prime crack driving force. In that aspect, this type of fatigue failure is more akin to plain fatigue.

The paper is organised as follows:

In section 2 two potential cases of mechanical loading that may have caused the fatigue failure are identified. Further, flange overheating may cause tensile residual stresses on the inside of the flange. Numerical simulations are performed to evaluate stresses in the flange caused by these load cases.

In section 3 it is shown that one of the mechanical load cases is likely to have caused fatigue initiation and final fracture. An overview estimation of the crack growth life is performed.

The analysis thus far established root causes and indicated required preventive actions. It was therefore employed in the failure investigation of the Swedish Accident Investigation Authority [2].

To further quantify the influence of misaligned brake blocks in general and specifically for the studied case, section 4 features an in-depth analysis of the influence of flange overheating on crack loading. The analyses show that the crack was likely to initiate before previous reprofiling and that final fracture was likely promoted by a tensile residual stress caused by severe flange overheating.

Finally, the results are summarised and commented in section 5.

The novel features of the study reported here and in [1] include the detailed assessment of this rare type of failure, and the employed combination of fracture analysis, thermomechanical simulations, and fatigue assessments. In particular, it relates to the innovative approach of evaluating the residual stress field from viscothermoplastic simulations and mapping it onto a fracture mechanics model. This analysis allowed to identify likely scenarios and root causes of this costly accident in a setting where many parameters are uncertain, and results are sensitive to changes in input set-up.

2. Operational loads and resulting stresses

To cause the fatigue failure in Fig. 1, a (cyclic) tensile stress at the inside of the flange is required. The three load cases in Fig. 3 that each will cause a tensile stress at the inside of the flange are studied. The load cases are here analysed separately using the finite element method as implemented in the commercial finite element software ABAQUS. The mechanical loads are not included in the analysis of the thermomechanical problem of braking since they only influence the state of stress at the back of flange during sharp curving conditions (see section 2.2) which should constitute a negligible portion of the duration of the braking action with displaced blocks. The interaction of the load cases is studied in detail in the fatigue analyses in section 4 in which residual stresses introduced by the thermal load case are combined with the stress variations introduced by the mechanical load case c.

2.1. Thermal loading and resulting residual stresses

The schematic loading presented in Fig. 3a features an offset brake block which will heat also parts of the wheel flange. Under normal operations, the flange is never heated by the brake block contact. The motivation to consider this non-standard thermal load case of a laterally displaced brake stems from the finding at the derailment site that a brake block had worn to conform to the tread–flange geometry, see [1]. If the heating and resulting constrained thermal expansion is sufficiently high to cause yielding, tensile residual stresses (in the circumferential direction) will form in the wheel rim (as expected at tread braking after cooling) but for our case also in the flange region of the wheel, which is extraordinary.

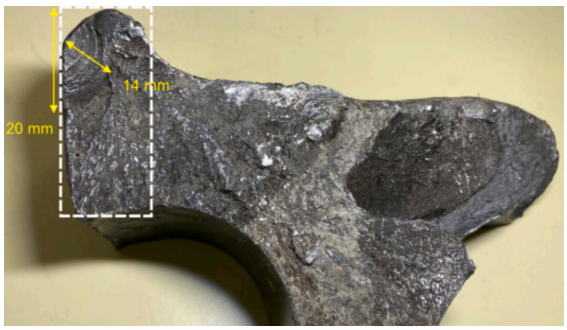

Fig. 1. Fatigue crack at inside of flange causing the failure.

Fig. 2. Blueing of the wheel in the radius below the tread.

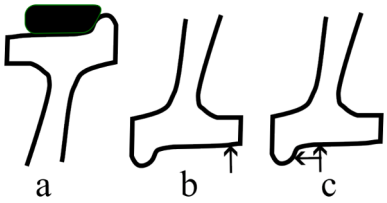

Fig. 3. Schematic representation of load cases. a) Thermal load induced by laterally displaced brake block. b) Mechanical load at the field side on wide track and/or on the inner rail when cornering. c) Mechanical loads at the flange side on the outer rail in a curve with flange contact.

The thermomechanical analysis (Fig. 4a) employs an axisymmetric model which previous studies [6] have shown to be a reasonable simplification. The model features 1735 eight node axisymmetric elements. Boundary conditions are indicated in Fig. 4a. The applied power is transferred to an evenly distributed heat flux q_{brake} [W/m^2] by dividing the power with the brake block contact area on the wheel. This evenly distributed surface heat flux is applied over tread and flange surfaces marked red in Fig. 4a.

Heating of the wheel here accounts for the laterally shifted brake block position that gives heating of parts of the wheel flange. Temperature-dependent thermal material properties are considered [7]. Cooling is accounted for through radiation and convection with parameters calibrated based on freight car temperature measurements [7]. More in detail, the cooling model has been experimentally calibrated by measured temperatures from field testing campaigns on freight wagons featuring braking at constant power and speed at the Velim test circuit in the Czech Republic, but also for conditions with varying braking power levels and speeds during commercial coal transports in North-Eastern South Africa. For the current analyses, the cooling influence of the axle is disregarded as it would have a minor effect on wheel rim temperatures and build-up of residual stresses.

A recently developed viscoplastic constitutive model is used for the simulation. The model has been calibrated using results from both isothermal and anisothermal testing to capture wheel steel behaviour at severe braking conditions for temperatures up to 750 °C. The model is of Chaboche-type and features e.g., thermal deterioration at elevated temperatures to capture reduction in yield strength

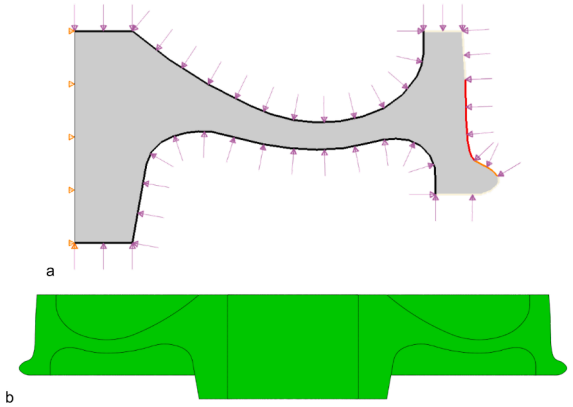

Fig. 4. FE-models. a) Termomechanical FE-model with thick black lines indicating cooling via convection and radiation, white lines indicating cooling via convection and reduced radiation (glossy surface), and red line indicating heat input and reduced convection and radiation accounting for parts of the surface covered by blocks. The hub is locked radially on the inside and axially on the flange side. b) Mechanical FE-model with imposed boundary conditions featuring a locked hub, and symmetry conditions applied to the relevant cross-sections. Loads are described in section 2.2.

as introduced by pearlite spheroidisation. For clarity, the material model is briefly presented below along with adaptions employed in the current study. A detailed presentation of the model is given in [8] along with experimental data used for calibration.

The plastic region is defined by the Mises yield criterion

$$f = \sqrt{\frac{3}{2}}|\sigma_{\text{dev}} - X| - (R + k) < 0 \tag{1}$$

Where σ_{dev} is the deviatoric stress, X the kinematic backstress, R the isotropic hardening stress and k the initial yield stress. The viscoplastic strain evolves as

$$\dot{\epsilon^p} = \dot{\lambda}\frac{\partial f}{\partial \sigma} = \frac{\eta(f)}{t_*}\sqrt{\frac{3}{2}}\frac{\sigma_{\text{dev}} - X}{|\sigma_{\text{dev}} - X|} \tag{2}$$

where t. is a material parameter controlling viscous behaviour and the Delobelle overstress function is $\eta(f) = \sinh\left(\langle\frac{f}{D}\rangle^n\right)$ with $D =$ 1 MPa for achieving correct units. The evolution of the isotropic hardening stress R is given by $\dot{R} = \dot{\lambda}b(Q - R)$, with Q determining hardening saturation and b the rate of hardening. The kinematic hardening uses a Chaboche decomposition, extended by including a static recovery effect to account for relaxation of stress, with the resulting evolution being

$$\dot{X}_i = \dot{\lambda}\left(\frac{2}{3}C_i - \gamma_i X_i\right) - \frac{\Lambda}{\tau_i}\left(\frac{|X_i|}{M_i}\right)X_i + \frac{1}{C_i}\frac{dC_i}{dT}\dot{T}X_i \tag{3}$$

With hardening constants C_i, saturation hardening γ_i, $X = \sum_{i=1}^{n} X_i$ and $\Lambda = 1 - \frac{\langle\dot{T}\rangle}{\dot{T}}$, with the latter introduced to prevent relaxation during straining. In the present work, three kinematic stresses are used, which was found sufficient at calibration of model parameters. In addition, it was found that the non-recoverable softening following pearlite spheroidization at high temperatures could be modelled by a time-dependent exponential function

$$\dot{P} = \rho(P_\infty - P) \tag{4}$$

where P is reduction in yield and hardening constants, where e.g., correction to the yield stress k is made as $k = k_{\text{virgin}}$ (1+ P), with k_{virgin} being the yield stress of the material prior to softening, and ultimate reduction is $P_\infty = -0.2$ after long time at 600 °C.

This material model has been extensively used for studying thermomechanical effects on wheel behaviour [9]. Yield strength and hardening parameters are in this study adapted to the current material AAR Class B through modifying the parameters used for the originally considered ER7 wheel steel material, based on differences in yield strength, see [10]. The most important modified material parameters are presented in Table 1. Remaining parameters can be found in [8]. To account for rim chilling, initial yield strength and hardening parameters are reduced linearly from the tread (of a new wheel) to a depth of 100 mm, after which no further change occurs. Maximum reduction is 20% [11].

For the studied train, a normal wagon braking its own weight down to Narvik provides an approximate braking power of $Q_{\text{brake}} =$ 30 kW for about 30 min. Since braking power may be unevenly distributed between wagons, and potentially influenced by brake malfunctioning, also higher brake power levels are investigated.

Temperature and residual stress in the circumferential direction after 30 min of braking with a total brake power of $Q_{\text{brake}} = 30,$ and 60 kW are shown in Fig. 5 and Fig. 6. Simulation results for thermal loads $Q_{\text{brake}} = 30, 40, 50$ and 60 kW are summarised in Table 2.

The brake load case 30 kW gives negligible tensile stresses in the area on the inside of the flange for the studied case featuring a laterally displaced brake block. It is therefore reasonable to assume that such braking in combination with previous wheel turning has removed the compressive residual stress that arises during rim chilling. This assumption is further supported by previous studies that indicate that tensile residual stresses after severe drag braking are found to be almost independent of initial stresses [12].

Only braking above some 50 kW results in significant residual stresses. This is a high heat power, but it should be noted that the residual stress at the wheel failure in principle corresponds to the highest braking power during the entire lifetime of the wheel since the last reprofiling. The reason is that the rolling contact does not (significantly) affect the residual stress state on the inside of the flange.

Table 1
Material parameters employed for AAR Class B wheel material.

T [°C]	E [GPa]	K [MPa]	C_1 [GPa]	C_2 [GPa]	C_3 [GPa]	Q [MPa]
RT	185	360	100	90	20	100
200	180	360	100	90	20	100
325	180	290	130	70	18	100
400	170	250	120	80	11	−5
500	165	130	120	80	7	−25
600	150	60	180	140	12	−30
750	170	40	70	5	1	−30

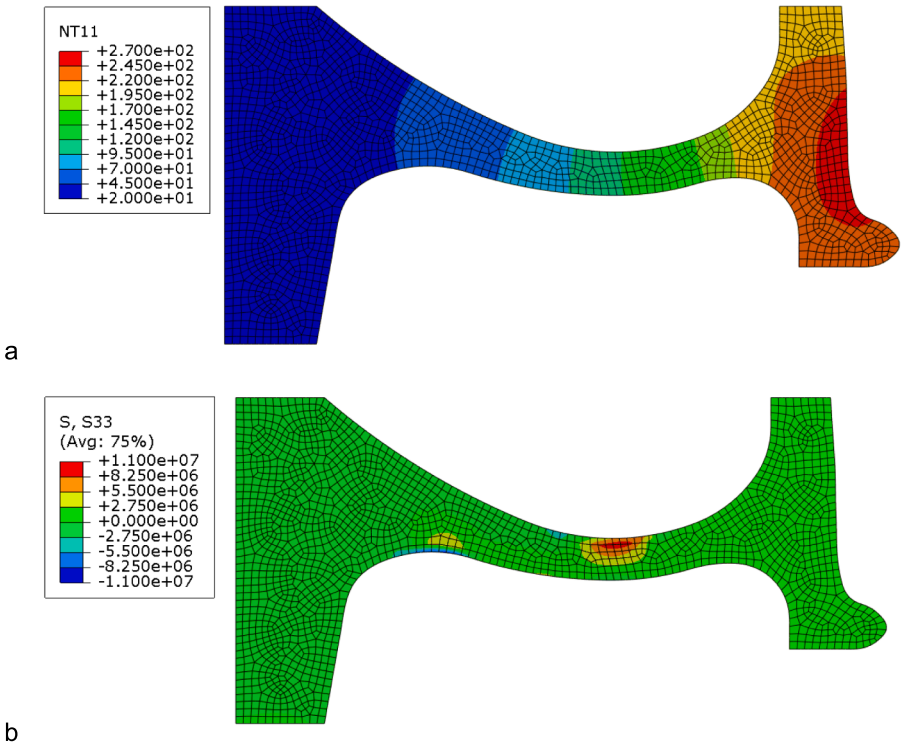

Fig. 5. Results for $Q = 30$ [kW]. a) Temperature at end of braking. b) Circumferential residual stress.

A summary of circumferential stress evolution during braking and cooling for the different power levels is shown in Fig. 7.

2.2. *Mechanical loading*

For mechanical analyses, the load cases in Fig. 3b and c will both induce bending of the flange giving tensile stresses at the back of the flange. A three-dimensional finite element model of half the wheel featuring 822 000 20 node isoparametric elements with full integration is used, see Fig. 4b where boundary conditions are defined. An elastic material model with $E = 200$ GPa and $\nu = 0.3$ is used. Loads are based on the wheel design standard EN13979-1 [13], with an employed axle load of 31 tonnes.

On the field side of the wheel (Fig. 3b) a vertical force $F = 1.25P = 191$ kN where P is the static wheel load, is applied 15 mm from the field side. On the flange side (Fig. 3c) a vertical force $F = 1.25P = 191$ kN is applied 27 mm from the flange side, and a lateral force $F = 0.6P = 91.2$ kN applied 14 mm above the rolling circle against the flange. The forces are distributed over surface nodes over a circular area with a radius of 1 cm, which is motivated by the necessity of avoiding local stress effects to interfere with the studied part of the flange, which would result if a lateral point force would be used in an elastic model setting. The lateral force is applied at a point 14 mm radially outside the rolling circle, which is 4 mm more than the 10 mm stipulated in EN13979-1. This choice is uncontroversial considering that it is well-known that the contact between wheel and rail can take place at more exterior positions on the flange than the one given in the standard. See e.g. [14], in which the contact point is up to 15 mm outside of the rolling circle for nominal profiles of wheel and rail. The load application point was in the present study chosen since it results in measurable higher stresses in the flange but has a negligible influence on wheel web fatigue (the focus of the standard). The increase can partially be explained by how the point load is transferred onto a load carrying area on the flange.

Examples of circumferential stresses for the load cases in Fig. 3b and c are shown in Fig. 8 and Fig. 9. In the circumferential section where the mechanical load acts, the field side load (Fig. 3b) produces compressive stresses on the inside of the flange, while the flange loads (Fig. 3c) produce tensile stresses. A few decimetres from this circumferential section, the conditions are reversed.

The mechanical load act on a “cold wheel”. Stresses during braking are expected to differ significantly only if regions of the wheel feature temperatures above some 400 °C when the yield strength starts to decrease significantly [15].

3. Fatigue failure

Given the evaluated stresses, an assessment is made whether these stresses are sufficient to trigger fatigue initiation, drive crack growth and cause final fracture. The simplified fracture mechanics assessment in section 3.2 is employed to assess whether the studied mechanical load cases are likely to have caused the fracture. This is complemented by a refined FE-analysis in section 4 to evaluate if a residual stress (caused by flange overheating) is required to cause final fracture (and also to quantify how it influences short crack

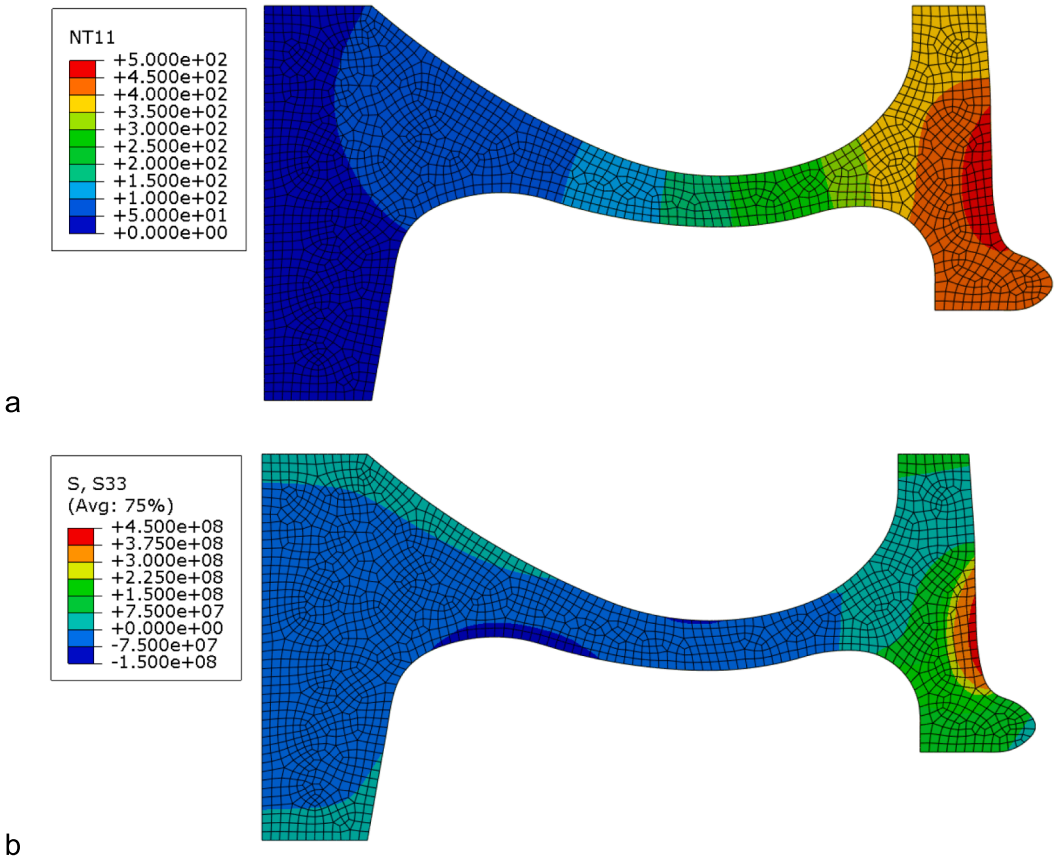

Fig. 6. Results for Q_{brake} = 60 kW. a) Temperature at end of braking. b) Circumferential residual stress.

Table 2
Max temperatures and stress magnitudes on the inside of the flange. Node positions shown in Fig. 6.

Braking load case	Max temperature on tread [°C]	Highest tensile stress on inside of the flange [MPa]
30 kW	267	1.0
40 kW	338	3.0
50 kW	420	28 (node 1), 16 (node 4)
60 kW	490	81 (node 1), 63 (node 4)

growth). The fatigue crack growth analysis in section 3.3 is used to assess how frequent inspections need to be, and to understand whether the crack might have existed even before the last reprofiling.

3.1. Fatigue initiation

Maximum and minimum (over a wheel revolution) stresses on the inside of the flange stemming from the two mechanical load cases b and c are reported in Table 3. Note that load cases b and c will never interact and that the yielding caused by the thermal loading during braking will result in a static residual stress field that will be superposed on these mechanical stresses.

An effective stress that accounts for the influence of the mean stress according to Smith–Watson–Topper, see e.g., [16], is calculated as

$$\sigma_{\mathrm{SWT}} = \sqrt{\sigma_{\max} \cdot \sigma_{\mathrm{a}}} \tag{5}$$

where the stress amplitude is calculated as

$$\sigma_{\mathrm{a}} = \frac{\sigma_{\max} - \sigma_{\min}}{2} \tag{6}$$

Under the assumption of negligible residual stress, i.e. $\sigma_{\mathrm{res}} = 0$, the stress magnitudes in Table 3 translate to stress amplitudes and

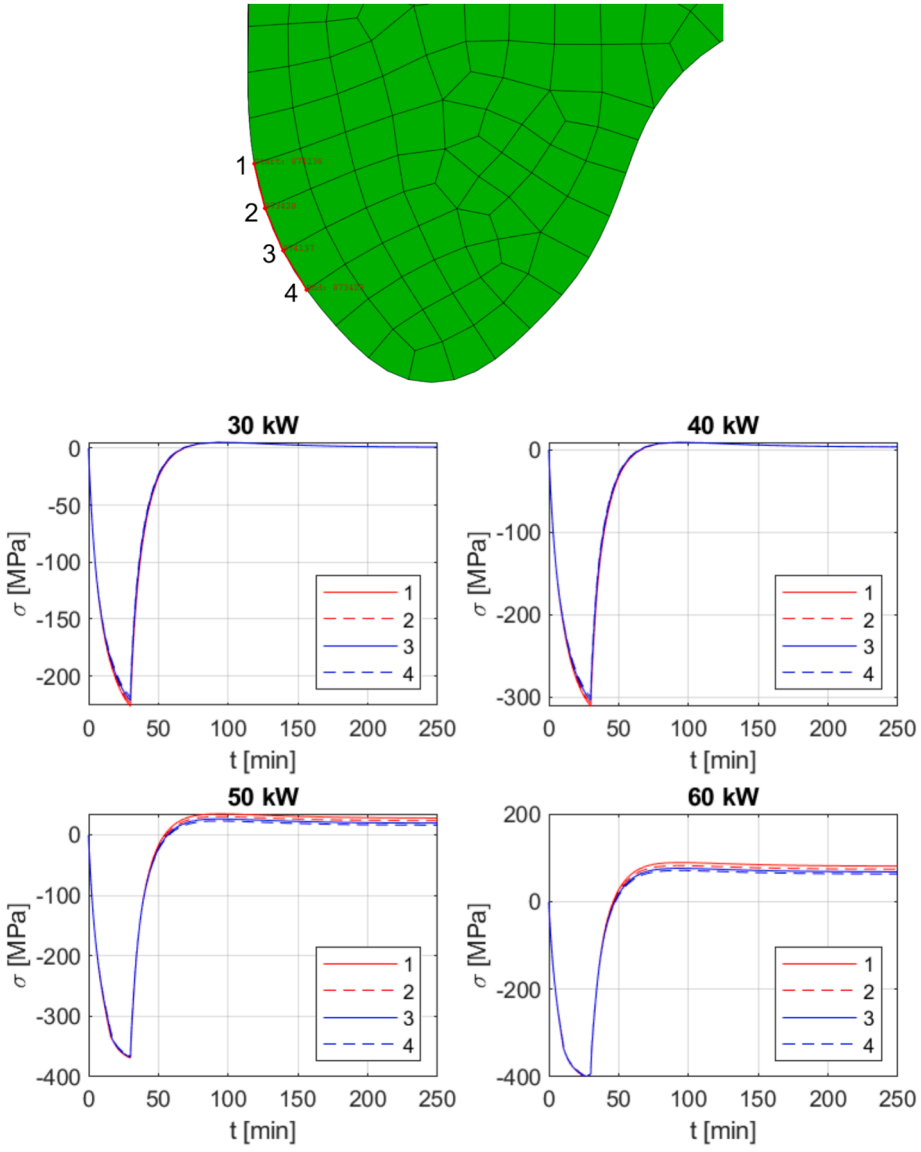

Fig. 7. Circumferential stress over time (during braking and subsequent cooling) for indicated nodes on the inside of the flange.

effective stresses according to Table 4.

The ultimate strength of the material on the tread is $\sigma_u \approx 1\,000$ MPa and in the body $\sigma_u \approx 835$ MPa [1]. This gives an unreduced fatigue limit of $\sigma_e \approx 0.5\sigma_u \approx 450$ MPa, see e.g., [16].

For fatigue to occur at the calculated effective stress magnitudes, a reduced fatigue limit, σ_{er}, is required, such that $\sigma_{SWT} > \sigma_{er} = m\sigma_e$ where m is a reduction factor due to surface roughness, loaded volume etc. For the two load cases in Fig. 3b and c, the required reduction factors for fatigue crack initiation to occur are $m_b = 60/450 = 0.13$ and $m_c = 160/450 = 0.36$, respectively with indices indicating the respective load case. With the high ultimate stress of the material and observed high surface roughness at the back of the flange [1], a reduction factor of $m \approx 0.3$ is not unreasonable, cf. [16]. This means that fatigue may have been initiated by a flange load (Fig. 3c) if surface damage was present, but most likely not by the field side load (Fig. 3b) since $m \approx 0.13$ is an unrealistically low reduction factor for the studied surface conditions.

Note that the position of initiation in Fig. 1 is closer to the flange top than the position of maximum stress. This may be due to larger surface damage higher up and/or a different point of application of the load in relation to the point of fatigue initiation than assumed. It can be noted here that reprofiling does not remove material in the area where the crack was initiated. Crack initiation and incipient growth may thus have occurred before the last reprofiling when the initiation point was more on level with the wheel tread.

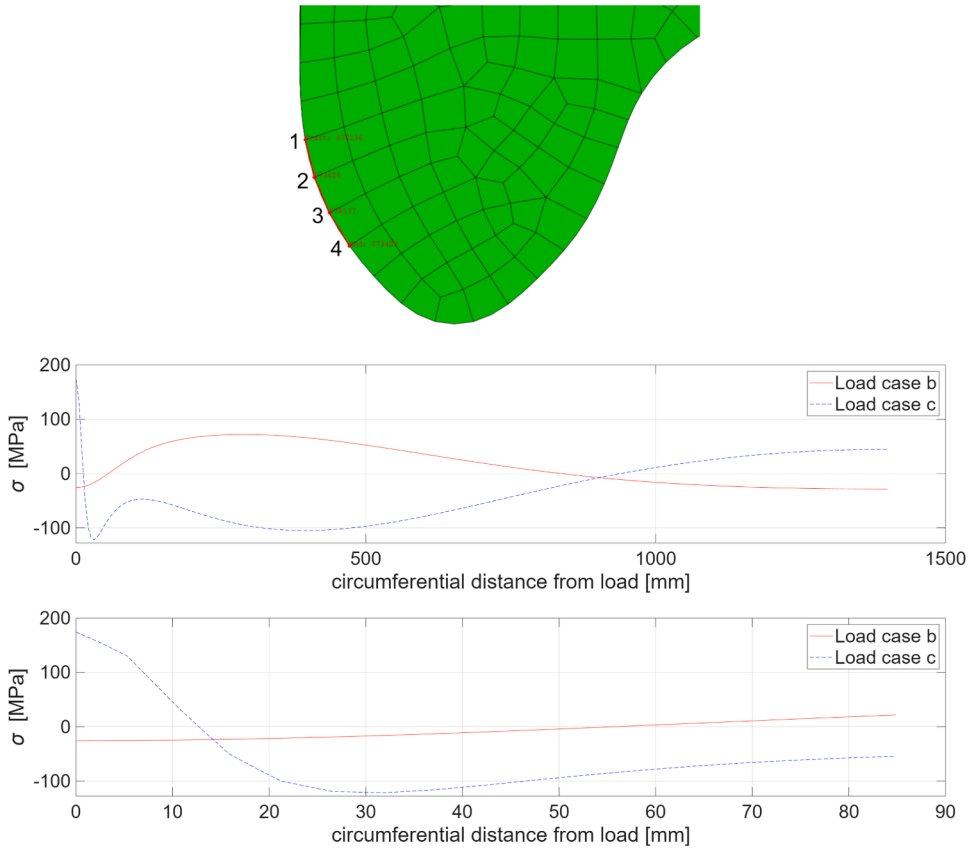

Fig. 8. Circumferential stresses in node 1 for load cases in Fig. 3b (load on field side) and c (load on flange side). Overview of load positions around half the wheel circumference and zoom-in of an area in the vicinity of the load.

3.2. Final fracture

The crack on the outside of the flange in Fig. 1 is studied. Using the elementary case in Fig. 10, the stress intensity factor for a quarter-circular corner crack can be estimated [17] as

$$K_{\mathrm{I}} = \frac{M}{\Phi}\sigma_0\sqrt{\pi a} \tag{7}$$

Here $\Phi = E(0) \approx 1.57$ where E is the complete elliptic integral of the second kind.

This is in principle equivalent to studying the area in Fig. 1 that is limited by a dashed white line. The influence of the remaining wheel rim, wheel disc, etc. is then neglected. In addition, a uniformly distributed nominal stress is assumed. These assumptions mean that the results should only be taken as an indication of whether crack growth and fracture are reasonable under the studied loads. More precise calculations of stress intensities are presented in section 4.

Estimated dimensions of the parameters in Fig. 10 based on Fig. 1 are $a = 14$ mm, $t = 24$ mm and $W = 50$ mm. These correspond to the width and height of the white dashed rectangle. With $a/t = 0.6$, case 9.59 in [17] gives $M \approx 1.37$ which with uniformly distributed nominal stress $\sigma_0 = 100$ MPa (taken lower than the maximum stress for load case c in Table 3 to roughly compensate for the stress gradient) gives the stress intensity

$$K_{\mathrm{I}} = \frac{1.37}{1.57}100\sqrt{\pi \cdot 0.014} = 18\,\mathrm{MPa}\sqrt{\mathrm{m}} \tag{8}$$

The fracture toughness of a number of material classes for freight wheels is listed in [10]. Selected values of $K_{\mathrm{Q}}^{\mathrm{RT}}$ (the dimension-dependent fracture toughness at room temperature used by railway industry when ASTM criteria for test dimensions are not fully met [18]) and $K_{\mathrm{V}}^{-20^\circ\mathrm{C}}$ (impact toughness at -20°C) from table 24 in [10] are compiled in Table 5. It is seen that for these materials (and units) $K_{\mathrm{Q}}^{\mathrm{RT}}/K_{\mathrm{V}}^{-20^\circ\mathrm{C}} \approx 8$.

In the accident report [19], impact toughness (K_{V}) at -20°C and -40°C are presented, see Table 6. Assuming that $K_{\mathrm{Q}}^{\mathrm{RT}}/K_{\mathrm{V}}^{-20^\circ\mathrm{C}} = 8$ also for the damaged wheel, the minimum value of $K_{\mathrm{Q}}^{\mathrm{RT}}$ can be estimated as $K_{\mathrm{Q,min}}^{\mathrm{RT}} \approx 8 \cdot 4.2 = 34\,\mathrm{MPa}\sqrt{\mathrm{m}}$. The minimum value is most

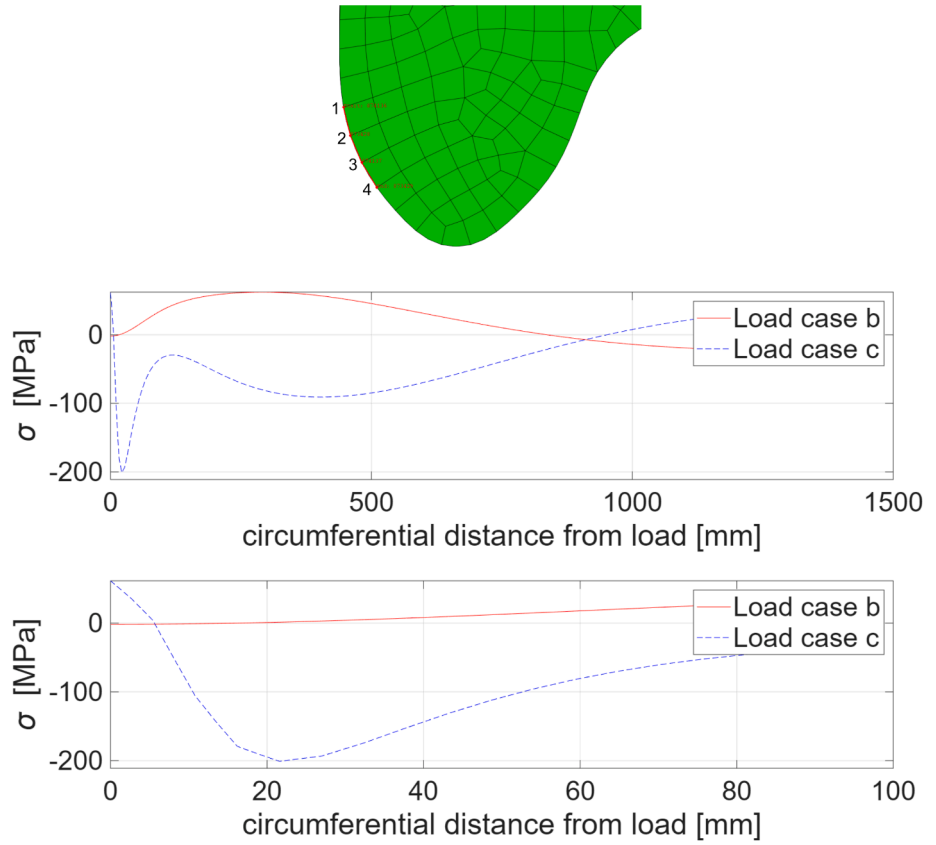

Fig. 9. Circumferential stresses in node 4 for load cases in Fig. 3b (load on field side) and c (load on flange side).

Table 3
Stress variations [MPa] on the inside of the flange.

node stress	1	2	3	4
$\sigma_{b,max}$	72	69	66	62
$\sigma_{b,min}$	–28	–28	–26	–25
$\sigma_{c,max}$	174	146	108	61
$\sigma_{c,min}$	–122	–145	–170	–201

Table 4
Fatigue stress on the inside of the flange [MPa].

node stress	1	2	3	4
$\sigma_{b,a}$	50	48	46	44
$\sigma_{b,SWT}$	60	58	55	52
$\sigma_{c,a}$	148	146	139	131
$\sigma_{c,SWT}$	160	146	123	89

interesting here since fracture usually occurs in weaker materials.

It is also seen that $K_V^{-40^\circ C}/K_V^{-20^\circ C} \approx 0.6$ for minimum values. If it is assumed that the decrease in fracture toughness between room temperature and the temperature at the time of fracture (about 0 °C) corresponds to the decrease in impact toughness between -20°C and -40°C, we get $K_Q^{0^\circ C} \approx 0.6 \cdot 34 = 20\,\text{MPa}\sqrt{\text{m}}$. Although this assumption can be discussed since the decrease is not a linear function of temperature, the calculations show that it is not unlikely that $K_I \approx K_Q^{0^\circ C}$ (implying fracture) under the studied conditions.

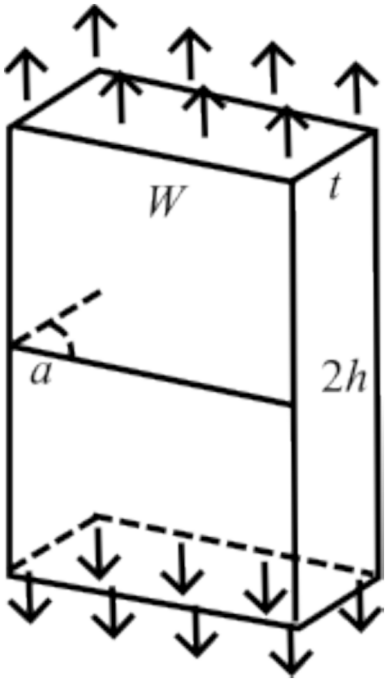

Fig. 10. Quarter-circular surface crack subjected to a uniform tensile stress.

Table 5
Average values of fracture toughness and impact toughness for freight wheel material classes.

classvalue	R7T	Class B	Class B+	Class C	Class C+
$K_Q^{RT}[MPa\sqrt{m}]$	90	60	51	50	45
$K_V^{-20^\circ C}[J]$	14	8	6	6	5
$K_Q^{RT}/K_V^{-20^\circ C}$	6,4	7,5	8,5	8,3	9

Table 6
Impact strength of the current wheel at different temperatures. From [19] test K401258.

	$K_V^{-40^\circ C}$	$K_V^{-20^\circ C}$	$K_V^{-40^\circ C}/K_V^{-20^\circ C}$
average	3.5	4.5	0.8
minimum	2.5	4.2	0.6

3.3. Fatigue crack growth

It is notoriously difficult to estimate the stress intensity factor threshold for crack growth. A rough estimate [19] is

$$\Delta K_{\text{th}} \approx 7\,\text{MPa}\sqrt{\text{m}} \tag{9}$$

For the current load cases with $\sigma_{\min} < 0$, a reasonable assumption is $\Delta K = K_{\max} - 0$, i.e., compressive stresses are not considered to contribute to crack growth.

For a crack radius $a = 2.4$ mm we get $a/t = 0.1$ and $M \approx 1.13$ which with nominal uniformly distributed stress $\sigma_0 \approx 100$ MPa gives the stress intensity

$$K_I = \frac{1.13}{1.57} 100\sqrt{\pi \cdot 0.0024} = 6\,MPa\sqrt{m} \tag{10}$$

A first estimate is therefore that cracks (and crack-like defects) deeper than some 2–3 mm will grow under the studied load.

An estimate of crack growth life is obtained by integrating Paris law

$$\frac{da}{dN} = C(\Delta K)^n \tag{11}$$

with $C = 5.8 \cdot 10^{-7}$ and $n = 3.7$ for ΔK in MPa and da/dN in meters per cycle estimated as that of Class B wheel steel heated to 750 °C and tested at room temperature [20]. The somewhat high temperature is selected in order to achieve conservative predictions with slightly faster crack growth than in the studied case.

With crack geometry according to Fig. 10 and a uniform cyclic nominal stress with the stress range $\Delta\sigma = (\sigma_{\max} - \max[\sigma_{\min}, 0]) = 100$ MPa, the number of cycles to failure as a function of initial crack length are presented in Fig. 11. An initial crack length of 2 mm corresponds to a life of approximately 5 000 cycles and an initial crack length of 3 mm to a life of approximately 3 000 cycles. These results are relatively independent of the K_Q magnitude.

The studied flange load implies hard flange contact with lateral over vertical force being $0.6/1.25 \approx 0.5$. This should only occur in sharp curves. Several load cycles may occur in such a curve, but the crack is only loaded in tension when flange contact occurs at a circumferential position that corresponds to the position of the crack.

Since compressive stresses are not considered to contribute to crack growth, a tensile residual stress in the flange will correspond to an increase in ΔK proportional to magnitude of the residual stress as long as $\sigma_{\min} \leq 0$. Further, the employed stress level corresponds to a worn, reprofiled wheel and are lower for a larger wheel diameter. The influence of the stress level on the crack growth life is given in Fig. 12.

In summary, it is not possible to estimate the service life of a 2–3 mm initial crack with any precision with the limited input data available. A first estimate, however, could be that a stress level as high as $\sigma_{0,\max} = 100$ MPa occurs a maximum of ten times per loaded trip as an average over the wheel's service life for a wagon with relatively poor running characteristics. More load cycles with hard flange contact should result in severe flange wear and thus early reprofiling. This would correspond to a few hundred loaded trips to failure, which takes months of operation. This rough life estimate will be further discussed in the following.

4. Detailed fracture mechanics analyses

To assess the accuracy of the simplified fracture mechanics analyses in sections 3.2 and 3.3, detailed elastic finite element analyses were carried out. The 3D finite element model of the wheel is shown in Fig. 13. Symmetry conditions are used for the wheel symmetry plane (except for the crack face) and the hub is fully clamped. Forces are as previously introduced at reference points from which the force is distributed to adjacent nodes over a specific radial distance from the point.

The residual stress field after severe braking that introduces tensile stresses in the flange area was evaluated in separate thermomechanical simulations. Considering that the crack will not influence the elastoplastic wheel response during braking, since the crack closes, the previously described viscoplastic material model can straightforwardly be employed. However, to account for the calculated residual stresses in a standard linear elastic fracture mechanics analysis, a novel scheme was developed for capturing the effects from the calculated residual stresses in a model featuring an elastic material. An optimisation routine using a genetic algorithm in MATLAB (Version R2025a) was hence employed to derive a fictive temperature distribution over the wheel rim with elastic material that resulted in a stress field resembling that derived in the elastoplastic thermomechanical analysis. This temperature field is in the wheel rim is derived using a superellipsoidal variation near the tread, a 2nd degree polynomial in the radial direction, and a 4th degree polynomial in the lateral direction. To this end, (fictive) temperatures were introduced on the cross-sectional area of the wheel rim in three parts to firstly relate to the superellipsoidal variation T^{super} given by the function

$$f(x,y,T) = \left(\left(\frac{r}{r_0}\right)^{2/e} + \left(\frac{z}{z_0}\right)^{2/e} \right)^{e/n} + \left(\frac{T^{\text{super}}}{T_0}\right)^{2/n} = 1 \tag{12}$$

where parameters e and n control the shape, T_0 gives temperature amplitude, r is the radial coordinate of the wheel, r_0 and z_0 give the centre points. This expression is suitable for capturing effects introduced by the local yielding of the wheel rim material seen in Fig. 5 and Fig. 6. To capture the total effect in the rim, this needs to be superimposed on a global stress variation (i.e., for the region $r > R_{\text{rim}}$, where R_{rim} is radial coordinate of the web-to-rim transition).

$$T^{\text{radial}}(r) = k_1(r - R_{\text{rim}}) + k_2(r - R_{\text{rim}})^2 \tag{13}$$

However, the braking also causes a plastic response in the wheel disc, that together with the residual stresses in the rim introduces a lateral stress variation when interacting with the curved disc shape of the wheel. This variation can be captured using

$$T^{\text{lateral}}(z) = m_1(z - Z_{\text{rim}}) + m_2(z - Z_{\text{rim}})^2 + m_3(z - Z_{\text{rim}})^3 \tag{14}$$

Here z is the axial coordinate of the wheel rim with Z_{rim} at the field side of the rim.

The fictive temperature given by $T(r,z) = T^{\text{super}}(r,z) + T^{\text{radial}}(r) + T^{\text{lateral}}(z)$ along with an assumed orthotropic thermal expansion in the wheel circumferential direction can reproduce the residual stress fields derived from braking simulations employing the viscoplastic material model. By this innovative method it is possible to quantify the effects of an overheated flange, stemming from an offset brake block position on fracture in a straightforward manner.

The crack geometry is explicitly modelled in the flange area with the finite element mesh refined in the vicinity of the crack. Stress intensities along the crack front are derived from evaluated J-integral magnitudes.

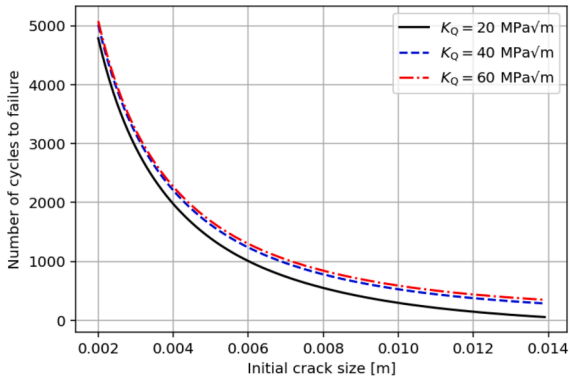

Fig. 11. Life span of a quarter-circular surface crack as a function of initial crack length for different fracture toughness magnitudes K_Q with $\Delta\sigma = 100$ MPa.

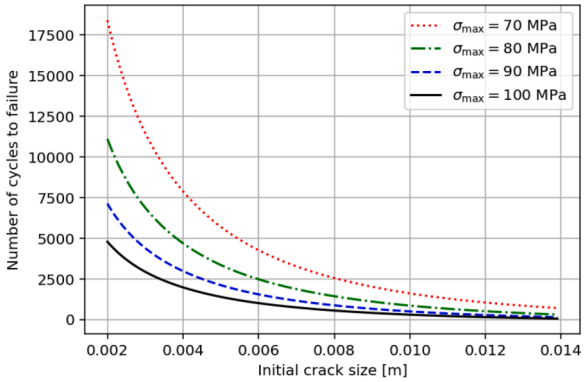

Fig. 12. Fatigue life of a quarter-circular surface crack as a function of initial crack length for different nominal stresses $\sigma_{0,max}$ with $K_Q = 20\,MPa\sqrt{m}$.

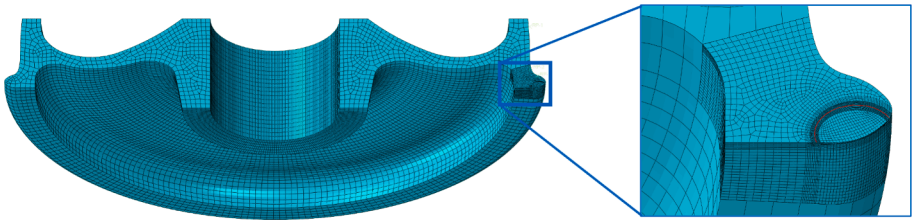

Fig. 13. Finite element model of wheel with flange crack.

Two crack geometries based on the measured geometry in figure 1 are studied.

- a small crack representing the early stage of growth on the inside face of the flange (depth 3 mm and half-length 3.7 mm)
- a large crack (depth 14 mm and half-length 10 mm) with a geometry resembling the crack near final brittle fracture of the wheel, see Fig. 1.

Calculated stress intensities for residual stresses from 60 kW braking with a laterally displaced brake block during 30 min, mechanical loads following section 2.2 with the addition of a case with lateral load increased by 50% are presented in Fig. 13. For the small crack positioned at the crack initiation point seen in Fig. 1, it is found that the stress intensities are lower than some 7 MPa$\sqrt{m}$, which means the crack would have grown very slowly, if at all, cf. equation (9). This is the case both for combined vertical and lateral loads according to the EN standard, and when the lateral load is increased by 50%. The main reason for this behaviour is that the stresses introduced by the mechanical forces do not result in high tensile stresses in the flange area where the crack is positioned. However, if one assumes that the small crack instead was initiated before last machining, here modelled using an offset crack geometry positioned 10 mm radially towards the hub without modifying the wheel geometry (see results for "Small crack$^{mod.}$" in Fig. 14) the

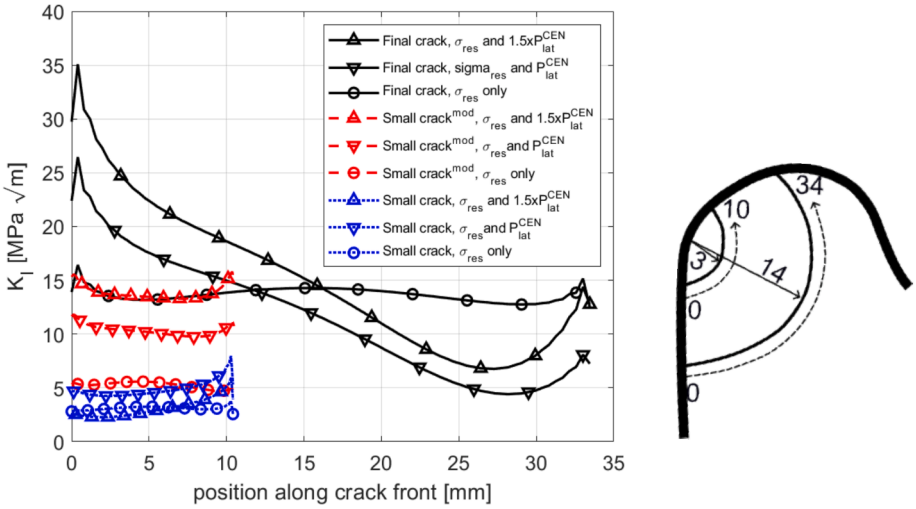

Fig. 14. Calculated stress intensities along crack fronts for (combinations of) residual stress, σ_{res} from 60 kW braking during 30 min, curving with standard loads, and curving with lateral load increased by 50%. Position coordinates along crack fronts are illustrated on the right for a small crack and the final crack. For the small crack results are also provided for a crack offset 10 mm towards the hub, denoted by "mod".

calculated stress intensities increase substantially. Here, already the EN standard load case gives stress intensities of about 10 MPa$\sqrt{m}$. The stress intensity magnitudes are rather constant along the crack front. The exceptions are at the edges where boundary effects increase the stress intensity but also introduce a state of plane stress which gives a higher fracture toughness. This means the crack is in balance and will propagate at roughly the same rate along the crack front. Increasing the lateral load by 50% increases the stress intensities by between 25% and 50% along the crack front. At this early stage of crack growth, this increase would however have to be sustained over a longer time to provide any substantial increase in crack growth rates. This would imply non-functioning steering of the axle. Due to the damage of the derailed bogie, it could not be established whether this was the case.

The results for the large crack, which resulted in the final fracture, show that the residual stress field in itself introduces a stress intensity of almost 15 MPa$\sqrt{m}$. The mechanical load further increases the stress intensities along the first 12 to 16 mm in the low part of the crack front with a peak at some 25 MPa$\sqrt{m}$. Note that exceeding the fracture toughness in one point (or a short section) along the crack front is not sufficient to trigger global fracture as stress intensities will be redistributed during crack growth. If the lateral load is increased by 50%, for example due to hard flange contact in a switch, the maximum stress intensity reaches 35 MPa$\sqrt{m}$ and exceeds 20 MPa$\sqrt{m}$ over a distance of some 8 mm at the lowest part of the crack. That a load somewhat above the norm load together with a tensile residual stress from 60 kW braking with a laterally displaced brake block during some 30 min should trigger a wheel fracture when the fracture toughness is on the order of 20 MPa$\sqrt{m}$ is therefore reasonable.

The stress intensity distribution along the crack front in Fig. 14 would imply that final fracture set off in the lower part of the crack, increasing the stress intensity at remaining parts of the crack front as the crack grew, which caused the fracture to progress radially and axially into the rim. This is consistent with the crack morphology in Fig. 1.

It can be noted that stress intensity magnitudes agree fairly well between analytical estimations and finite element simulations given that the numerical simulations include residual stresses due to 60 kW braking during 30 min. This implies that conclusions from chapter 3 hold.

5. Concluding remarks

The analyses above of wheel failure setting out from a fatigue crack on the inside of the flange show that:

- At the stress levels that arise ($\sigma_{SWT} \approx 160$ MPa) at flange contact, fatigue initiation is likely if the flange surface has been severely scratched or similar. The assumption of high surface roughness on the inside of the flange is supported by the presence of scratches on the inside of the flange on the opposing wheel as shown in [1,19].
- Cracks should continue to grow further if they are deeper than a few millimetres. As shown in section 4, this would likely require a crack position corresponding to crack initiation before the last reprofiling.
- Residual stresses and overloads have a large influence on final fracture, but a smaller influence on fatigue initiation. Residual stresses have a large influence on crack growth, while the influence of single overloads on crack growth is small.
- Blueing of the wheel disc (see [1], [19]) and the discovery of a brake block worn against the flange indicate thermal overloading of the flange since the last reprofiling. FE-simulations indicate that a mechanical overload and a residual stress corresponding to roughly 60 kW braking for some 30 min with a laterally displaced brake block caused the final fracture. The same effect could be achieved at lower brake power levels if heating was more localised towards the flange than presumed.

- Based on simulation results the time for a small crack to grow to final failure is on the order of several months. As discussed above, it is likely that the crack started growing before the last reprofiling, which would correspond to a crack growth life (from a depth of around 3 mm) of at least 21 months, see [1]. As described in [1], the fatigue crack surface was too damaged to allow for striation analysis which could verify this estimation.

The stress levels are (even when additional residual stresses and overloads are taken into account) close to the strength levels, which suggests that several (or probably all) of the negative influencing factors — worn profile, low fracture toughness, scratched inside of flange, high load including residual stresses in the flange — must interact to cause a fatigue failure. This is reasonable since this type of failure is very uncommon. That the stress is close to the fatigue limit on wheels with worn profiles is supported by the presence of microcracks on the inside of the flange of some such wheels as discussed in [1,19].

The investigation shows the importance of controlling defects on the inside of the flange. This has been implemented in stricter inspection routines. Further, the identification of this uncommon failure type provides input to wheel design and maintenance limits.

In addition to the above conclusions, the paper presents a novel method on how a residual stress field in a wheel, quantified by FE-simulations featuring a viscoplastic material model, can be fitted using a superellipsoidal function, with some minor adaptions, so that an linear elastic fracture mechanics model can readily be employed for assessing the loading of a crack using standard FEM.

The study of cracks in railway wheels is an important field of studies that lately has attracted attention because of high profile accidents such as the one presented here, but the method presented could also be extended for example to simulate the conditions of the accident that closed down the Gotthard base tunnel in August 2023 [21].

CRediT authorship contribution statement

Anders Ekberg: Writing – original draft, Methodology, Investigation, Conceptualization. **Tore Vernersson:** Writing – review & editing, Methodology, Investigation, Conceptualization. **David Hjertsén:** Writing – review & editing.

Declaration of competing interest

The authors declare that they have no known competing financial interests or personal relationships that could have appeared to influence the work reported in this paper.

Acknowledgements

The work is part of the activities within the CHARMEC centre of excellence in railway mechanics (www.chalmers.se/charmec). Parts of the research is funded by the Swedish Accident Investigation Authority, and parts under the European Union's Horizon Europe research and innovation programme under grant agreements Nos: 101101966 (Iam4Rail), 101102001 (R2DATO) and 101102009 (TRANS4M-R).

Data availability

No data was used for the research described in the article.

References

[1] David Hjertsén, Anders Ekberg, and Tore Vernersson. 2025, Railway wheel failure caused by flange crack, Part 1: Background and failure analysis (2025) Submitted for publication.
[2] Jonas Bäckstrand, Mikael Hillbo, Lars Dahlin, Urspårning med godståg 9914 på Malmbanan (in Swedish: Derailment with freight train 9914 on the Iron Ore Line) (2025), The Swedish Accident Investigation Authority. https://shk.se/sok-utredningar/sparbunden-trafik/2023-12-20-ursparning-med-godstag-9914-pa-malmbanan.
[3] Eric E Magel, Rolling contact fatigue: a comprehensive review (2011) US Department of Transportation, Federal Railroad Administration, Technical report DOT/FRA/ORD-11/24. https://railroads.dot.gov/sites/fra.dot.gov/files/fra_net/89/TR_Rolling_Contact_Fatigue_Comprehensive_Review_final.pdf.
[4] Anders Ekberg, Bengt Åkesson, Elena Kabo, Wheel/rail rolling contact fatigue–Probe, predict, prevent, Wear 314 (1-2) (2014) Doi: 10.1016/j.wear.2013.12.004.
[5] S. Caprioli, T. Vernersson, A. Ekberg, Thermal cracking of a railway wheel tread due to tread braking–critical crack sizes and in fluence of repeated thermal cycles, Proceedings of the Institution of Mechanical Engineers, Part f: Journal of Rail and Rapid Transit 227 (1) (2013), https://doi.org/10.1177/0954409712452347.
[6] S. Teimourimanesh, T. Vernersson, R. Lundén, Modelling of temperatures during railway tread braking: Influence of contact conditions and rail cooling effect, Proceedings of the Institution of Mechanical Engineers, Part f: Journal of Rail and Rapid Transit 228 (1) (2014), https://doi.org/10.1177/0954409712465696.
[7] Tore Vernersson, Thermally induced roughness of tread braked railway wheels: part 2: modelling and field measurements, Wear 236 (1-2) (1999) Doi: 10.1016/S0043-1648(99)00261-6.
[8] Eric Voortman Landström, Erika Steyn, Johan Ahlström, Tore Vernersson, Thermomechanical testing and modelling of railway wheel steel, International Journal of Fatigue 168 (2023) Doi: 10.1016/j.ijfatigue.2022.107373.
[9] Eric Voortman Landström, Thermomechanics of tread braking – Braking capacity of railway wheels, Doctoral thesis, Department of Mechanics and Maritime Sciences, Chalmers University of Technology, Gothenburg, Sweden, 2024.
[10] A Ghidini, M Diener, J Schneider, Wheels for freight cars – development and applications for heavy haul service (2010) Lucchini RS.
[11] Eric Voortman Landström, Tore Vernersson, Roger Lundén, Improved modelling of tread braked wheels using an advanced material model, In Proceedings EuroBrake 2022.

[12] Ali Esmaeili, Tore V Vernersson, Nikas Dimitrios, Magnus Ekh, High temperature tread braking simulations employing advanced modelling of wheel materials, In Proceedings IHHA 2015.
[13] European committee for standardization, EN13979 Railway applications - Wheelsets and bogies - Monobloc wheels – Technical approval procedure - Part 1: Forged and rolled wheels (2024),.
[14] K. Karttunen, E. Kabo, A. Ekberg, A numerical study of the influence of lateral geometry irregularities on mechanical deterioration of freight tracks, Journal of Rail and Rapid Transit 226 (2012), https://doi.org/10.1177/09544097124451.
[15] J. Ahlström, E. Kabo, A. Ekberg, Temperature-dependent evolution of the cyclic yield stress of railway wheel steels, Wear 366 (2016), https://doi.org/10.1016/j.wear.2016.04.002.
[16] Norman Dowling, Stephen Kampe, Milo Kral, Mechanical Behavior of Materials. 5th ed. (2019) Pearson.
[17] Y Murakami, ed.. Stress intensity factors handbook, vol. 3 (1992) Pergamon press.
[18] European committee for standardization, EN 13262 railway applications – wheelsets and bogies – wheels – product requirements (2020).
[19] David Hjertsén, Undersökning av tåghjul J-18/23 (in Swedish: Investigation of train wheel), Report no TEK24-0032 (2024) Element materials technology AB.
[20] Lorenzo Ghidini, Angelo Mazzù, Michela Faccoli, Assessing the impact of thermal loading from brake shoes on microstructure and mechanical properties in various railway wheel steels: a comparative study, In Proceedings of the sixth international conference on railway technology: research, development and maintenance (2024) https://www.researchgate.net/profile/Lorenzo-Ghidini/publication/386236432_Assessing_the_impact_of_thermal_loading_from_brake_shoes_on_microstructure_and_mechanical_properties_in_various_railway_wheel_steels_a_comparative_study/links/67497f42359dcb4d9d3fe9e0/Assessing-the-impact-of-thermal-loading-from-brake-shoes-on-microstructure-and-mechanical-properties-in-various-railway-wheel-steels-a-comparative-study.pdf..
[21] The Swiss Safety Investigation Body SUST, Final report on the derailment of a freight train in the Gotthard Base Tunnel, 10 August 2023 in Faido (TI), Report no 2023081002.